ELSEVIER

Contents lists available at ScienceDirect

Nuclear Inst. and Methods in Physics Research, A

journal homepage: www.elsevier.com/locate/nima



Full Length Article

Optical transmission characterization of fused silica materials irradiated at the CERN Large Hadron Collider



S. Yang ^{a,b}, A. Tate ^{a,b}, R. Longo ^{a,*}, M. Sabate Gilarte ^c, F. Cerutti ^c, S. Mazzoni ^c, M. Grosse Perdekamp ^a, E. Bravin ^c, Z. Citron ^d, B. Kühn ^e, F. Nürnberg ^e, B. Cole ^f, J. Fritchie ^{a,b}, I.Gelber ^d, M. Hoppesch ^a, S. Jackobsen ^c, T. Koeth ^g, C. Lantz ^a, D. MacLean ^{a,j}, A. Mignerey ^g, M. Murray ^h, M. Palm ^c, M. Phipps ^a, S. Popescu ^{h,k}, N. Santiago ^a, S. Shenkar ^d, P. Steinberg ⁱ

- ^a Department of Physics, University of Illinois, 1110 W. Green St., Urbana IL 61801-3080, USA
- b Department of Nuclear, Plasma and Radiological Engineering, University of Illinois, 1110 W. Green St., Urbana IL 61801-3080, USA
- c CERN, CH-1211, Geneva 23, Switzerland
- d Ben-Gurion University of the Negev, Department of Physics, Beer-Sheva 84105, Israel
- e Heraeus Quarzglas GmbH & Co. KG, Kleinostheim, Germany
- ^f Columbia University, Nevis Laboratories, Irvington, NY 10533, USA
- g University of Maryland, Department of Chemistry and Biochemistry, College Park, MD 20742, USA
- h University of Kansas, Department of Physics, Lawrence, KS 66045, USA
- ⁱ Brookhaven National Laboratory, Upton, NY 11973, USA
- ^j Currently with Fermi National Accelerator Laboratory, Batavia, IL, USA
- k IFIN-HH Bucharest, 077125, Romania1

ARTICLE INFO

Keywords: FLUKA Radiation damage Fused silica Optical transmission

ABSTRACT

The Target Absorbers for Neutrals (TANs) represent one of the most radioactive regions in the Large Hadron Collider. Seven 40 cm long fused silica rods with different dopant specifications, manufactured by Heraeus, were irradiated in one of the TANs located around the ATLAS experiment by the Beam RAte of Neutrals (BRAN) detector group. This campaign took place during Run 2 p+p data taking, which occurred between 2016 and 2018. This paper reports a complete characterization of optical transmission per unit length of irradiated fused silica materials as a function of wavelength (240 nm–1500 nm), dose (up to 18 MGy), and level of OH and H₂ dopants introduced in the manufacturing process. The dose delivered to the rods was estimated using Monte Carlo simulations performed by the CERN FLUKA team.

1. Introduction

Fused silica materials are widely used in a variety of optical applications such as lenses [1] and telecommunications [2] due to their excellent light transmission over a wide range of wavelengths, from the ultraviolet (UV) to the infrared [3–5]. Fused silica is composed of pure silicon dioxide, SiO_2 , in amorphous (non-crystalline) form [6,7]. The concentration of impurities like Al, Ca, Na, K, Mg, and Ti is typically smaller than 0.015 ppm [8] in fused silica. Due to its high purity, fused silica has excellent radiation resistance against coloration compared to other glassy materials, such as fused quartz. The number of absorption sites is correlated with the concentration of impurities in the material, which trap charge carriers induced by radiation, resulting in the production of color centers [9–11]. For these reasons, fused silica

is utilized in several applications designed to operate in radiation environments, including aerospace technology [12] and particle detectors at accelerator facilities [7,13–15].

The CERN Large Hadron Collider (LHC) is the world's highest-energy particle accelerator [16]. With an upgrade of the injectors started during Long Shutdown (LS) 2, the accelerator officially began its transition towards the High-Luminosity (HL) era [17,18]. The HL upgrade will be completed by the end of 2028, resulting in a higher collision rate, thereby increasing the radiation levels in the experiments and the accelerator tunnel. Some of the most critical regions of the accelerator, in terms of radiation, are the Target Absorbers for Neutrals (TANs in the current LHC implementation, to be upgraded to TAXNs for the HL-LHC [19]), which are the radiation absorbers for neutral particle debris produced by beam collisions in the ATLAS [20] and CMS [21] interaction regions (IRs). Detectors that are installed and operated in

E-mail address: riccardo.longo@cern.ch (R. Longo).

On leave.

^{*} Corresponding author.

Fig. 1. Schematic of the arm 8-1 TAN at the LHC during 2016–2018 p+p runs. The numbers and colors in the right part of the figure identify the position of the rods in the BRAN prototype detector. Material specifications of the rods, as well as the maximum integrated doses accumulated in them, are shown in Table 1.

the TA(X)N, including the Beam RAte of Neutrals (BRAN) [22] and the Zero-Degree Calorimeters (ZDCs) [23,24] of ATLAS and CMS, will experience unprecedented radiation levels in the HL-LHC. For this reason, a Joint Zero-degree Calorimeter Project (JZCaP) [25] between the ATLAS and CMS ZDC groups was started to identify radiation-hard materials capable of withstanding the doses expected in the HL era. Given the similar challenges to be faced, the JZCaP and the BRAN group started a collaboration to study the radiation hardness of materials to be used for the HL upgrade of both detectors. Since both groups plan on constructing Cherenkov-based detectors, these studies were targeted at fused silica materials.

The radiation characterizing the TA(X)N is unique since it is primarily due to high-energy products generated in the showering of very forward neutral particles in the absorber. To study the radiation damage induced by this highly-energetic hadronic and electromagnetic cocktail, a new BRAN prototype detector, equipped with fused silica rods, hereafter referred to as "BRAN rods", was installed in one of the IR1 TANs during the 2016–2018 p+p run.

The BRAN rods were doped with different concentrations of hydroxyl (OH) and hydrogen (H₂) to study dopants' impact on the radiation hardness of fused silica. Given the nature of Cherenkov light, in particular its wavelength (λ) spectra, falling as $1/\lambda^2$, it is of great interest to study the radiation hardness of the radiator over a wide wavelength range extending into the UV region.

The beam energy reached by the LHC in Run 2 (2016–2018) provided an opportunity to study the radiation hardness of fused silica over a wide dose range, up to \sim 18 MGy. Detailed FLUKA [26–28] simulations were performed by the CERN FLUKA group, to estimate the dose accumulated in each part of the TAN, including the fused silica rods, during the Run 2 p+p irradiation campaign. FLUKA results enabled the possibility of correlating different rod segments with the doses accumulated in them. The radiation damage was evaluated via measurements of the optical transmission of the irradiated fused silica samples compared to those of an un-irradiated sample (hereafter referred to as "control"). This manuscript presents a study of the optical transmission of irradiated fused silica as a function of various factors, including wavelength of light, radiation dose, and material composition.

The paper is structured in the following way: Section 2 describes the BRAN prototype detector, the irradiation setup in the TAN and the corresponding FLUKA simulations used to estimate the dose accumulated in the BRAN rods. Section 3 provides the details of the optical transmission measurements, while Section 4 discusses the data analysis procedures. Results are presented and discussed in Section 5. Finally, conclusions are given in Section 6.

2. Irradiation setup of the BRAN prototype detector and FLUKA simulations

Fig. 1 shows a scheme of the BRAN prototype detector installed in the TAN on arm 8-1 of the ATLAS experiment during Run 2. The prototype detector was inserted in the TAN only during p+p runs, and is

made of three copper plates parallel to the beam propagation direction. A total of 8 slots are carved out in the copper, corresponding to a maximum occupancy of 8 fused silica rods. The cylindrical rods were manufactured by Heraeus Quarzglas [29] and had a length of 40 cm and a diameter of 1 cm. Further description of the experimental setup can be found in [30].

The rods were characterized by different levels of OH and $\rm H_2$ dopants, chosen to investigate the impact of material composition on the glass radiation hardness. Fused silica rods were inserted only in slots from 1 to 6 (see Fig. 1 for the layout), while positions 7 and 8 remained empty, allowing for the study of Cherenkov light yield in air (results not discussed in this paper). The specifications of each rod are listed in Table 1.

This work makes use of FLUKA simulations to evaluate the doses accumulated in the BRAN rods. FLUKA is a general-purpose Monte Carlo code for particle interaction and transport over a wide energy range. It has been benchmarked against recorded doses in the LHC and has been shown to have excellent agreement with data [31,32]. Remarkable results were also achieved in the description of other aspects of the radiation environment in the accelerator, such as the activation of materials after Run 2 [30]. Using dedicated FLUKA simulations of the TAN region, it was possible to study the profile of the doses accumulated in the fused silica rods during Run 2. Because the detector experienced different beam crossing configurations in 2016 and 2017, two simulations were performed using the following settings:

- 1. p+p run in 2016: $-180~\mu rad$ half crossing angle and integrated luminosity of 38.5 fb⁻¹.
- 2. p+p run in 2017: +140 µrad half crossing angle and integrated luminosity of 50 fb⁻¹.

These values correspond to the integrated luminosity delivered to ATLAS during 2016 and 2017 [33]. Fig. 2 shows FLUKA results for the x-z profile of the dose deposited in the TAN during the p+p runs in both 2016 and 2017. The right-handed coordinate system used in the simulations is defined as follows: x points outside the LHC ring in the horizontal plane, z is along the ATLAS detector axis towards the right side, and y is in the vertical direction towards the surface. The profile was extracted at the y coordinate of the maximum dose value registered in the TAN. Note that, since the 2017 and 2018 runs were characterized by the same beam crossing configuration, the dose map for 2018 was computed by rescaling the 2017 dose map using the ratio of the integrated luminosity delivered to ATLAS in the two years. Thanks to FLUKA, it was also possible to characterize the spectrum of particles impinging on the rods during the irradiation time. An example is shown in Fig. 3. More details about the irradiation setup and the FLUKA simulations can be found in Ref. [30].

3. Optical transmittance measurements

The detailed dose profile of each rod provided by the FLUKA simulations enables the possibility of studying the transmittance of a given fused silica materials at different irradiation levels. As reported in

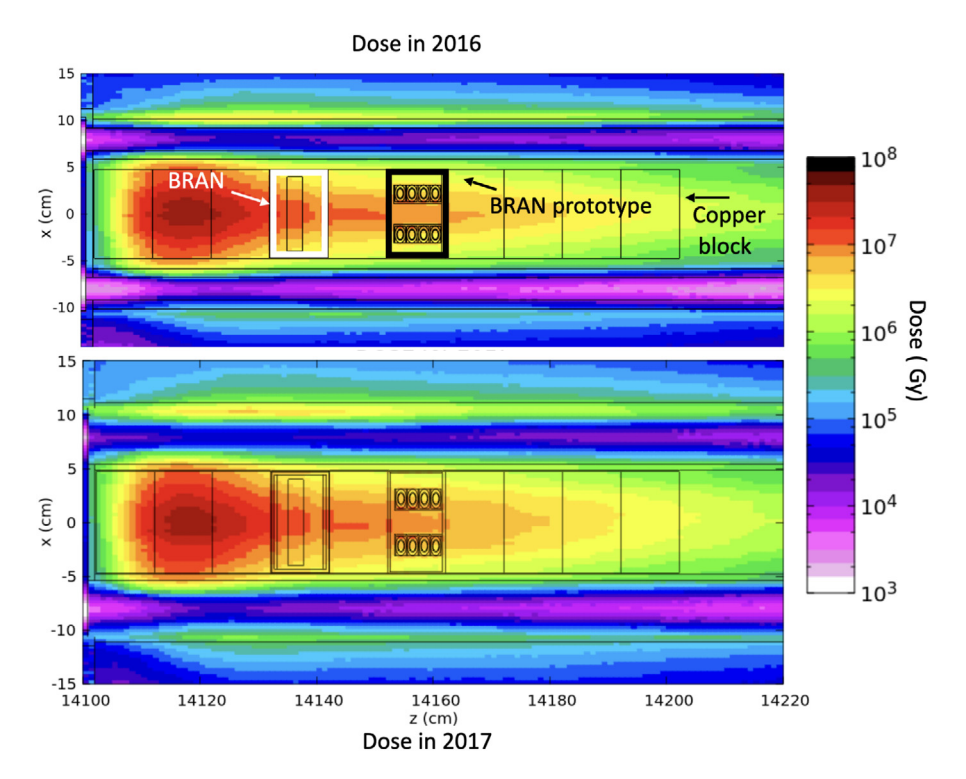


Fig. 2. Accumulated dose x-z profile in the TAN in 2016 (upper) and in 2017 (lower) p+p runs, respectively. The BRAN prototype is highlighted by the black box, while the white box marks the position of the BRAN detector. The integrated luminosity was 38.5 and 50 fb⁻¹ in 2016 and 2017, respectively.

Table 1Specifications of the irradiated fused silica rods. The number and color of each rod correspond to a given position in the BRAN prototype detector during the irradiation, as shown in Fig. 1. The same color scheme will be used when comparing results obtained from different materials. Rods 3a and 3b were placed in the same slot but in different periods.

BRAN Position	Irradiation Period	Max. Dose [MGy]	Material	H ₂ [mol/cm ³]	OH [ppm]
Control	None	0	Spectrosil 2000 (High OH, Mid H ₂)	7.20e17	1120
1	04/2016- 12/2018	18	Spectrosil 2000 (High OH, Mid H ₂)	7.20e17	1120
2	04/2016- 12/2017	10	Spectrosil 2000 (High OH, Mid H ₂)	7.20e17	1120
3a	04/2016- 12/2016	5	Spectrosil 2000 (High OH, High H ₂)	2.80e18	1000
3b	04/2017- 12/2018	16	Spectrosil 2000 (High OH, Mid H ₂)	7.20e17	1120
4	04/2016- 12/2017	9	Spectrosil 2000 (High OH, H ₂ free)	0	1011
5	04/2016- 12/2017	8	Suprasil 3301 (Low OH, High H ₂)	3.00e18	15
6	04/2016- 12/2018	17	Suprasil 3301 (Low OH, H ₂ free)	0	14

Ref. [30], the dose accumulated in a single rod spans over four orders of magnitude along the vertical direction. Therefore, by cutting the rods into 1 cm segments, it was possible to form sub-sets of 40 samples, each characterized by the same material composition and different irradiation levels.

A digital caliper was used to measure the maximum (t^{max}) and the minimum (t^{min}) length of a given sample. These lengths were determined by rotating the sample 360° within the caliper. The average cut length (t_s) was calculated as

$$t_s = \left(\frac{t^{max} + t^{min}}{2}\right). \tag{1}$$

More details regarding the sample preparation can be found in Ref. [30].

During the cutting process, the blade introduces roughness on the cut surface. A refractive index matching liquid was used to reduce the effect of the surface on the optical transmission measurements. Series AA liquid from Cargille Laboratories, characterized by a refractive index value of 1.456 at 589.3 nm at 25.0 °C [34], was chosen for the measurement. A comparison between the refractive index of Series AA and fused silica is shown in the left panel (a) of Fig. 4. A Suprasil 3001 fused silica cuvette was used to contain the samples and the liquid during the measurement. The right panel of Fig. 4 shows an example

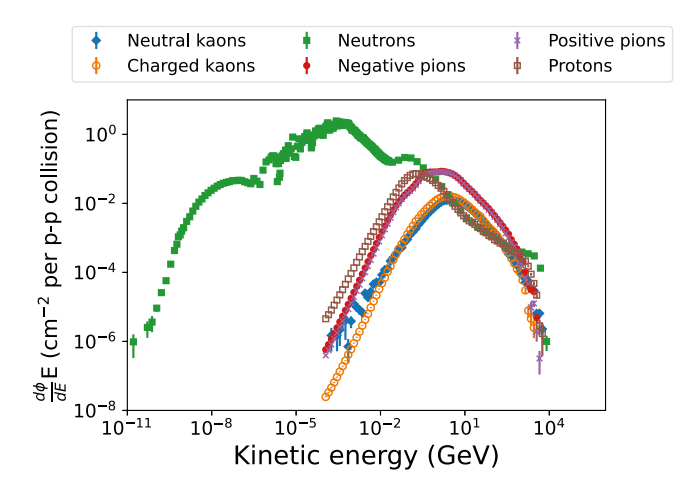


Fig. 3. Fluence per p+p collision of different particle species impinging on the bottommost 5 cm of Rod 1 in 2016, extracted from FLUKA simulations. In the 2016 crossing-angle configuration, this portion of the rod corresponds to the highest radiation levels registered in the material [30].

of a sample after the cut (b) and inserted in the cuvette with refractive index matching liquid (c).

The transmittance of the samples was measured using a Varian Cary 5000 [35] spectrophotometer, capable of performing measurements over a large wavelength range. This work presents results from 240 to 1500 nm. The sampling interval was 1 nm, the average measurement time was 0.1 s, and the spectral bandwidth was 2 nm. Air was used as a reference to calibrate the instrument for all the measurements presented in this study, including the fused silica samples and the refractive index matching liquid. For each measurement, the sample was immersed in the refractive index matching liquid in a cuvette placed in the Cary's built-in cuvette holder. The sample was centered with respect to the optical beam. A schematic of the experimental setup is shown in Fig. 5.

4. Data analysis

The Beer–Lambert law [36] was used to correct for the effects of the refractive index matching liquid on intensity measurements in this study. The attenuation coefficient of the Series AA liquid, α_l , was calculated using the intensity of the light measured with only liquid in the cuvette.

The corrected intensity \hat{I} of a sample was then calculated as

$$\hat{I} = Ie^{\alpha_l t_l},\tag{2}$$

where I is the measured intensity and t_l is the longitudinal length of the liquid (\sim 1.05 cm) between a sample and the cuvette. The transmittance T of the sample was calculated by comparing the corrected intensity to that of the control sample [37]. To allow for an unbiased comparison between different samples, the transmittance per unit length \bar{T} of each sample was calculated by its attenuation coefficient α_s , which was determined using

$$\alpha_s = \frac{-1}{t_s} \ln(T). \tag{3}$$

Then, the attenuation coefficient was used to evaluate \bar{T} as:

$$\bar{T} = TC, \tag{4}$$

where C is a correction factor given by

$$C = e^{-\alpha_s(t_n - t_s)}. (5)$$

In the last formula, t_n represents the arbitrary unit length chosen for the normalization and was set to 1 cm in this study. Readers interested in the derivation of the uncertainty on \bar{T} can refer to Appendix A.

5. Results and discussion

This section first presents the measured transmittance as a function of dose and wavelength. A correlation between these two variables and the radiation damage experienced by the fused silica material, namely its transmittance degradation, is observed. Then, subsets of the BRAN rod sample results are selected based on their $\rm H_2$ and OH levels to analyze the dopants' impact on fused silica's radiation hardness at different dose levels. Note that "transmittance" in the following sections refers to the transmittance per unit length (\bar{T}) .

5.1. Transmittance degradation as a function of dose and wavelength

To correlate transmittance with the dose received by each rod segment, the whole simulation geometry was divided using a mesh (reflected by the resolution in Fig. 2). The deposited energy and error were computed for each mesh element by FLUKA. To calculate the dose of each rod segment, the dose registered in all cells within a segment was averaged, and the associated uncertainty was computed using standard error propagation.

Fig. 6 shows the transmittance for Rods 3a, 3b, 4, 5, and 6 as a function of the received dose and the wavelength. Among the different Spectrosil (high OH) rods available with an intermediate level of $\rm H_2$ dopants, Rod 3b was chosen for the analysis because its position is consistent with that of Rod 3a. As expected, the transmittance decreases as the accumulated dose in the samples increases. In addition to the dose dependence, the largest transmittance degradation is observed in the UV region (<400 nm). Therefore, although the wavelength of the measurements goes to 1500 nm, the wavelength range in the figure was limited to a range of interest for typical photomultiplier applications, e.g. up to 650 nm. Fig. 7 presents the transmittance versus dose in the UV region, where the highest amount of transmittance degradation is observed.

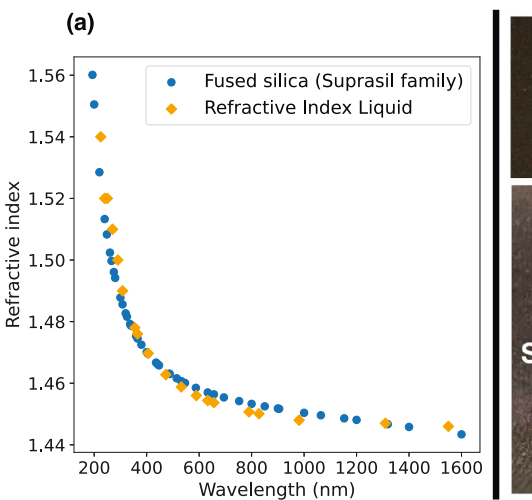
The transmittance of each rod was plotted as a function of dose for five different wavelengths, in increments of 40 nm from 240 to 400 nm. Results at 360 and 400 nm show minimal attenuation, even at 10 MGy, suggesting an excellent radiation hardness of fused silica above these values independent of the dopant levels. The highest level of degradation is observed at 240 nm, the lower limit of the wavelength spectra, for all materials studied. However, distinct attenuation patterns can be observed for rods characterized by different dopant levels, suggesting an effect of OH and $\rm H_2$ concentration on the fused silica's radiation hardness. Among all the rods, Rod 3a shows the lowest transmittance degradation in the UV region.

5.2. Impact of OH and H_2 dopant level on radiation hardness of fused silica

Different subsets of the BRAN samples were selected to investigate the effects of specific dopants. To simplify comparisons between the chosen subsets, the results at 240 nm, showing the largest radiation damage among all the materials, will be used in the following section to discuss the dopants' effect on the radiation hardness of fused silica. Further comparisons at 280 and 320 nm can be found in Appendix B.

The OH impact, independent of the $\rm H_2$ level, was analyzed by comparing Rod 6 (Suprasil 3301, Low OH) and Rod 4 (Spectrosil 2000, High OH), see Fig. 8. Both materials show similar transmittance behavior, but less degradation is observed for Suprasil 3301 at a given dose value up to 3 MGy. After ~1 MGy of irradiation, Spectrosil 2000's transmittance reaches a plateau of around 10%, while Suprasil 3301 continues to degrade beyond that dose level, ultimately reaching a transmittance of a few percent above 10 MGy.

An analogous study on the impact of OH doping when the fused silica is doped with H_2 was performed by looking at results obtained for Rod 5 and Rod 3a, as shown in Fig. 9. These two rods are characterized by a comparable level of H_2 , but different concentrations of OH. For doses >1 MGy, it is evident that Rod 3a experienced less transmittance



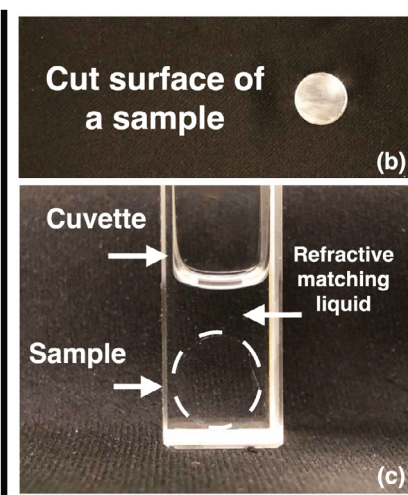


Fig. 4. (a) Refractive index comparison between fused silica (Suprasil family) and the chosen Series AA refractive index matching liquid. (b) The rough surface of a cut sample. (c) The sample immersed within the refractive index matching liquid in the fused silica cuvette.

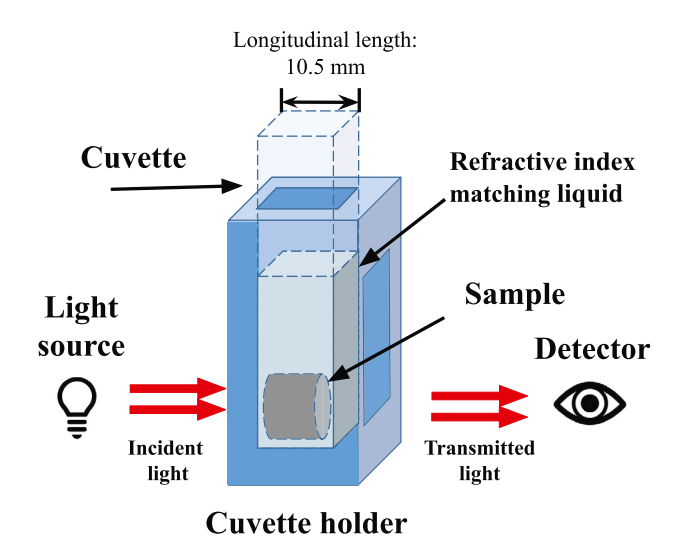


Fig. 5. Schematic drawing of the optical transmission measurement setup.

degradation than Rod 5. This trend indicates that a high concentration of OH can help in deferring the degradation when the fused silica is doped with a high concentration of H_2 . Overall, OH dopant concentration has a much smaller impact on the transmittance degradation compared to the concentration of H_2 dopant.

To further support this observation, two studies comparing rods with different levels of $\rm H_2$ at low and high OH were carried out. Results for the low OH case (Suprasil 3301) are shown in Fig. 10, where Rod 5 (High $\rm H_2$) and Rod 6 ($\rm H_2$ free) are compared. After 10 MGy of irradiation, the optical transmission of 240 nm light is reduced to a few % for both materials. However, it is interesting to note that the behavior of the transmittance degradation as a function of received dose varies based on the dopant. Rod 6 exhibits a gradual loss starting from the kGy scale, while Rod 5 shows little transmittance loss up to 500 kGy, but then rapidly degrades and reaches values compatible with a transmittance of zero around 10 MGy, while the $\rm H_2$ free rod tends to maintain a few % transmittance even beyond 15 MGy of irradiation.

Fig. 11 shows the results for the high OH case (Spectrosil 2000). Rod 3a (high H₂) exhibits minimal transparency losses between 0.1 and 1 MGy, while the optical transmittance of Rod 3b (mid H₂) remains at

only a few %. Increasing the concentration of H_2 by a factor of 4 helps to defer the dose turn-on value for the transmittance degradation by two orders of magnitude. Rod 4, without H_2 doping, exhibits gradual optical losses starting from the kGy range, with a transmission of approximately 0.1 between 0.1 MGy and 10 MGy. Rod 3b reaches full opacity at 240 nm around 1 MGy, without the plateau seen in Rod 3a.

6. Conclusions

A BRAN prototype detector containing different types of fused silica rods, doped with various levels of $\rm H_2$ and OH, was irradiated during LHC Run 2. The detector was installed in the TAN located in sector 8-1 of the ATLAS long straight section during the 2016–2018 p+p run. Thanks to detailed FLUKA simulations of the accelerator lattice from the ATLAS interaction point up to the TAN, it was possible to evaluate the dose accumulated in the rods. The dose in the rods was found to vary by four orders of magnitude along the vertical direction, allowing for an analysis of the radiation-induced optical attenuation in different fused silica materials across a wide dose range.

This manuscript presents a full characterization of the optical transmission of irradiated fused silica as a function of wavelength, received dose, and OH and $\rm H_2$ concentration. The irradiation of the fused silica rods was the result of a high-energy particle cocktail produced by the showering of very forward neutral particles originating from p+p collisions at IP1. This environment sets our analysis apart from the majority of previous fused silica analyses, where only neutrons, typically from a nuclear reactor, or photons, from lasers or other sources, were used to irradiate the materials.

For all the rods analyzed, most radiation damage appeared in the UV region, with the transmittance losses becoming more severe at lower wavelengths, while very limited transmittance degradation was observed in the wavelength region above 400 nm. $\rm H_2$ loading was observed to help in countering optical transmission degradation in irradiated fused silica. The benefit of $\rm H_2$ doping tends to fade away beyond certain radiation levels depending on $\rm H_2$ and OH concentrations. Once damage in the fused silica starts to appear, the transmittance of $\rm H_2$ -doped fused silica degrades faster compared to fused silica without any $\rm H_2$ load, where a saturation trend is observed. Similar observations were made in [39] by irradiating different fused silica materials using high-energy UV radiation.

The results presented in this paper highlight the incredible potential of fused silica for optical applications in highly-radioactive environments. The experimental method used for the transmission analysis was

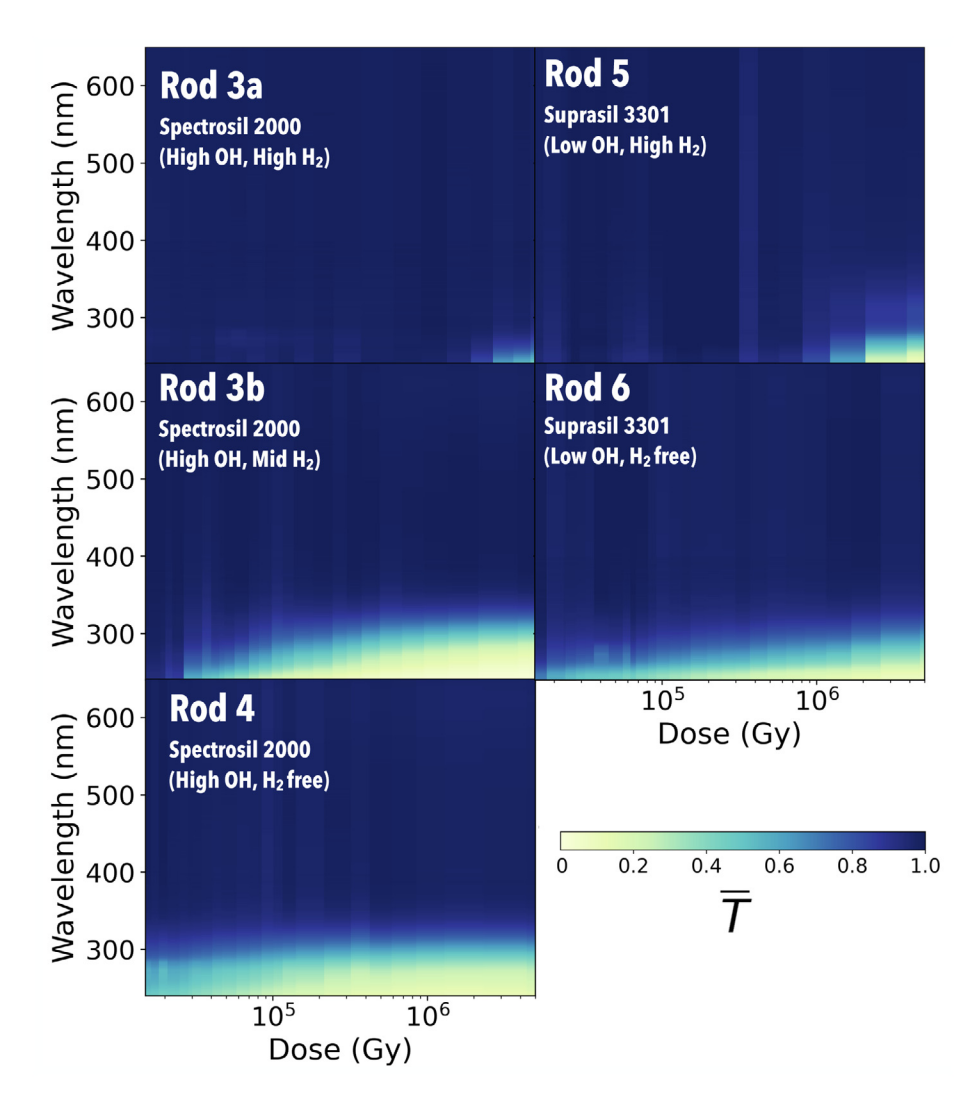


Fig. 6. Transmittance as a function of dose and wavelength for Rods 3a, 3b, 4, 5 and 6. The vertical axis represents the wavelength of the transmittance measurement. The horizontal axis displays the dose received by each sample, estimated using FLUKA. Note that the horizontal axis was limited to the dose range experienced by all rods, 1.5×10^4 to 5×10^6 Gy, and the vertical one, displaying wavelength, was restricted to 240–650 nm. The upper limit was chosen as a function of the typical primary sensitivity range of common photomultiplier tube's photocathodes [38].

developed after irradiation, introducing additional uncertainties due to the sample preparation and the use of the refractive index matching liquid. Additionally, the Run 2 irradiation campaign was limited by the luminosity delivered by the LHC in between 2016 and 2018.

Run 3 at the LHC offers an invaluable opportunity to carry out a new irradiation campaign thanks to specific grooves manufactured into the new BRAN-D detector, that was installed in the TAN at ATLAS and CMS in January 2022. The expected accumulated dose in the samples will surpass the one presented in this paper by at least one order of magnitude, given the higher integrated luminosity that the LHC is planned to deliver in Run 3 and the position of the BRAN-D closer to the shower maximum in the TAN. The experience gained during the Run 2 analysis was also exploited to achieve better sample preparation prior to the insertion in the LHC. This effort will streamline the analysis process and help to reduce experimental uncertainties in the transmittance measurement. The extraction of the samples from the LHC is foreseen by the end of Run 3, in 2025. In the shorter term, an irradiation campaign at the Soreq Nuclear Research Center which is complementary in the total dosage and has a different particle composition will be used for further analysis.

Declaration of competing interest

The authors declare that they have no known competing financial interests or personal relationships that could have appeared to influence the work reported in this paper.

Data availability

Data will be made available on request.

Acknowledgments

We would like to thank Dr. Mohammad Amdad Ali, from the Materials Research Laboratory at UIUC, for useful discussions. This work is in part supported by the National Science Foundation, United States, Grants no. PHY-1812377, PHY-1812325 and PHY-2111046, and by the U.S-Israel Binational Science Foundation, Grant no. 2020773.

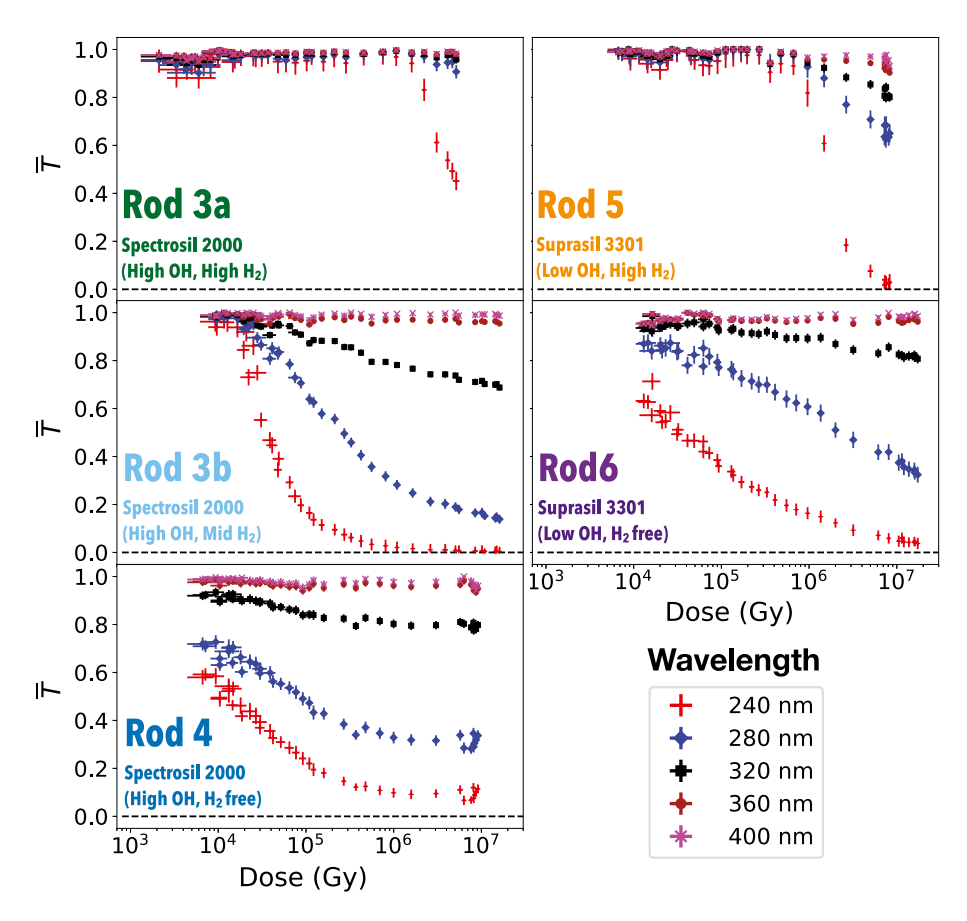


Fig. 7. Transmittance of Rods 3a, 3b, 4, 5 and 6 as a function of dose for five different wavelengths, in increments of 40 nm from 240 to 400 nm. The vertical axis represents the transmittance. The horizontal axis displays the dose received by each sample, estimated using FLUKA.

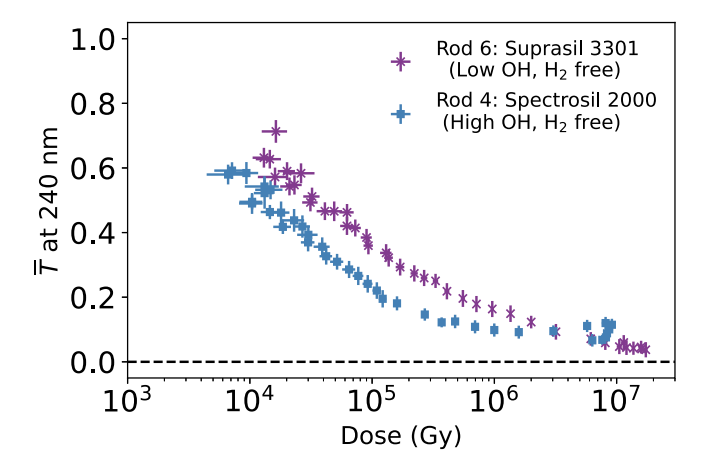


Fig. 8. Comparison of the transmittance at 240 nm between Rod 6 (Suprasil 3301, Low OH level and $\rm H_2$ free) and Rod 4 (Spectrosil 2000, High OH and $\rm H_2$ free) at different dose levels.

Appendix A. Uncertainty estimation

This study identified two primary sources of uncertainty, one introduced by the attenuation correction described in Section 4, and the other related to the systematic error due to positioning and alignment variation of samples in each measurement.

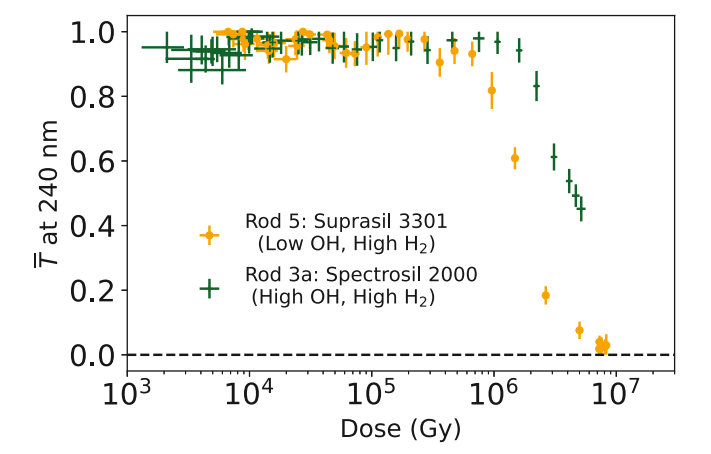


Fig. 9. Comparison of the transmittance at 240 nm between Rod 5 (Suprasil 3301, Low OH and High $\rm H_2$) and Rod 3a (Spectrosil 2000, High OH and High $\rm H_2$) at different dose levels.

The attenuation coefficient α_l of the liquid can be calculated as

$$\alpha_l = \frac{-1}{t_c} \ln(I_l), \tag{A.1}$$

where t_c is the longitudinal length of the cuvette and I_l is intensity of the light measured with only liquid in the cuvette. The corresponding

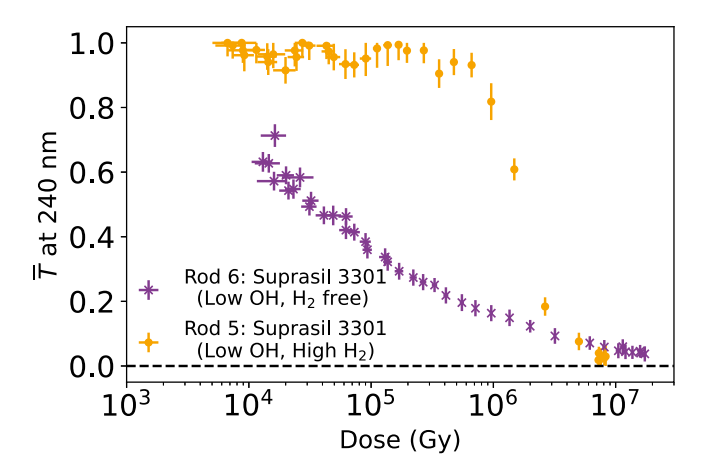


Fig. 10. Comparison of the transmittance at 240 nm between Rod 6 (Suprasil 3301, Low OH level and $\rm H_2$ free) and Rod 5 (Suprasil 3301, Low OH and High $\rm H_2$) at different dose levels.

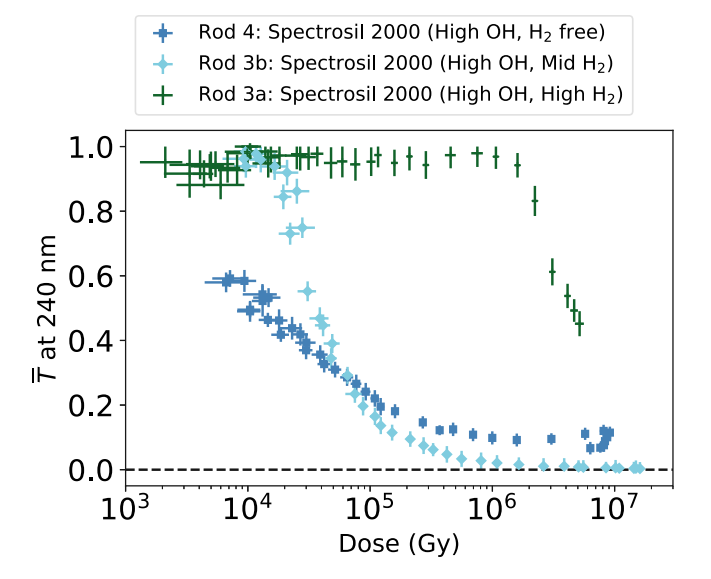


Fig. 11. Comparison of the transmittance at 240 nm between Rod 4 (Spectrosil 2000, High OH and H_2 free), Rod 3b (Spectrosil 2000, High OH and Mid H_2), and Rod 3a (Spectrosil 2000, High OH and High H_2) at different dose levels.

uncertainty σ_{α_i} was calculated as

$$\sigma_{\alpha_l} = \sqrt{\sigma_{I_l}^2 \left(\frac{-1}{I_l t_c}\right)^2 + \sigma_{t_c}^2 \left(\frac{\ln I_l}{t_c^2}\right)^2},$$
(A.2)

where σ_{I_l} is estimated using the standard deviation of 10 measurements with only liquid in the cuvette, and σ_{t_c} is the uncertainty on the length of the cuvette specified by the manufacturer, 0.05 mm.

The uncertainty on the corrected intensity calculated in Eq. (2), hereafter referred to as $\sigma_{\hat{I}}$, can be derived using standard error propagation:

$$\sigma_{\hat{I}} = \hat{I} \sqrt{(\alpha_l t_l)^2 \left[\left(\frac{\sigma_{\alpha_l}}{\alpha_l} \right)^2 + \left(\frac{\sigma_{t_l}}{t_l} \right)^2 \right] + \left(\frac{\sigma_I}{I} \right)^2}, \tag{A.3}$$

where σ_I is the uncertainty on the sample's intensity measurement and σ_{t_I} is the uncertainty on the longitudinal length of the liquid in the measurement. The attenuation caused by the liquid is affected by the uncertainty on the liquid thickness, σ_{t_I} , that was assumed to be equal

to

$$\sigma_{t_i} = t^{max} - t^{min}. \tag{A.4}$$

This assumption provides a conservative uncertainty on the corrected intensity. Note that the Cary 5000 spectrophotometer does not provide the uncertainty on measurements so σ_I was not available and assumed to be negligible. However, the largest contribution to σ_I comes from variations between each measurement, including the sample positioning and fluctuations in the spectrophotometer performance. In this analysis, such effects are accounted for by evaluating a systematic uncertainty associated with the transmittance results' reproducibility, which will be described later in this section.

The uncertainty on the transmittance of the sample, σ_T , can be expressed as

$$\sigma_T = T \sqrt{\left(\frac{\sigma_{\hat{I}}}{\hat{I}}\right)^2 + \left(\frac{\sigma_{\hat{I}_u}}{\hat{I}_u}\right)^2},\tag{A.5}$$

where $\sigma_{\hat{I}}$ and $\sigma_{\hat{I}_u}$ are the uncertainty on the corrected intensity of the sample and the control sample computed by using Eq. (A.3), respectively. The uncertainty σ_{α_s} on the sample's attenuation coefficient was computed as

$$\sigma_{\alpha_s} = \sqrt{\sigma_T^2 \left(\frac{-1}{Tt_s}\right)^2 + \sigma_{t_s}^2 \left(\frac{\ln T}{t_s^2}\right)^2},\tag{A.6}$$

where σ_{t_s} is the uncertainty on the sample's length, assumed to be the same as σ_{t_l} . Finally, the uncertainty $\sigma_{\bar{T}}$ on the transmittance per unit length calculated using Eq. (4) was evaluated as

$$\sigma_{\bar{T}} = \sqrt{\sigma_T^2 C^2 + \sigma_t^2 (TC\alpha_s)^2 + \sigma_{\alpha}^2 (TC(t_s - t_n))^2}$$
(A.7)

The systematic error resulting from variations introduced by sample positioning in each measurement due, for instance, to different rotations of the samples in the cuvette or thickness of liquid upstream/downstream of the sample, was also evaluated. A set of representative samples were selected based on their length and position in the rod, using the following procedure. First, the 40 samples obtained from each rod were grouped in batches of 10 consecutive samples each. Then, the samples characterized by the maximum and minimum lengths were picked within each of these groups, resulting in 8 samples for each 40 cm long rod. The control and each selected sample were measured ten times. For each measurement, the sample's orientation within the holder was varied by randomly rotating and flipping the sample.

Every measurement of the selected sample was paired with ten control measurements to calculate the corresponding transmittance (T), generating 100 transmittance results per selected sample. At each wavelength, the maximum and minimum transmittance values among the 100 results were obtained for each selected sample, and then the difference between the two extremes was computed. For each rod, at every wavelength, the maximum difference among the eight samples was then taken as a conservative estimate of the systematic error and propagated together along with the attenuation error to compute the final uncertainty on the transmittance per unit length (\bar{T}) .

Appendix B. Comparison of transmittance of fused silica characterized by different OH and $\rm H_2$ dopant level at 280 and 320 nm

See Figs. B.12-B.15.

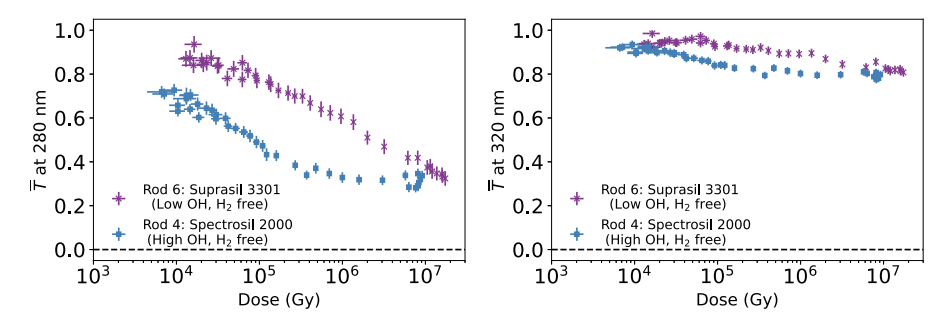


Fig. B.12. Comparison of the transmittance at 280 nm (left) and 320 nm (right) between Rod 6 (Suprasil 3301, Low OH level and H₂ free) and Rod 4 (Spectrosil 2000, High OH and H₂ free) at different dose levels.

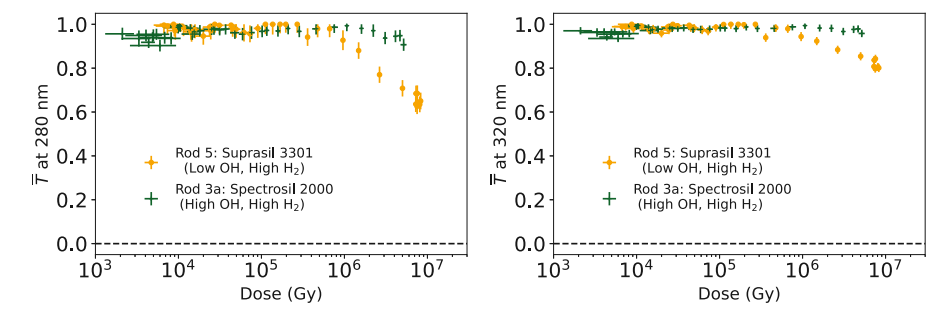


Fig. B.13. Comparison of the transmittance at 280 nm (left) and 320 nm (right) between Rod 5 (Suprasil 3301, Low OH and High H₂) and Rod 3a (Spectrosil 2000, High OH and High H₃) at different dose levels.

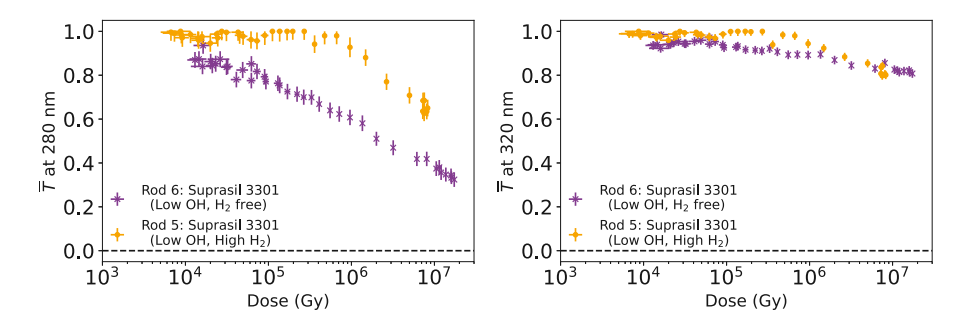


Fig. B.14. Comparison of the transmittance at 280 nm (left) and 320 nm (right) between Rod 6 (Suprasil 3301, Low OH level and H₂ free) and Rod 5 (Suprasil 3301, Low OH and High H₃) at different dose levels.

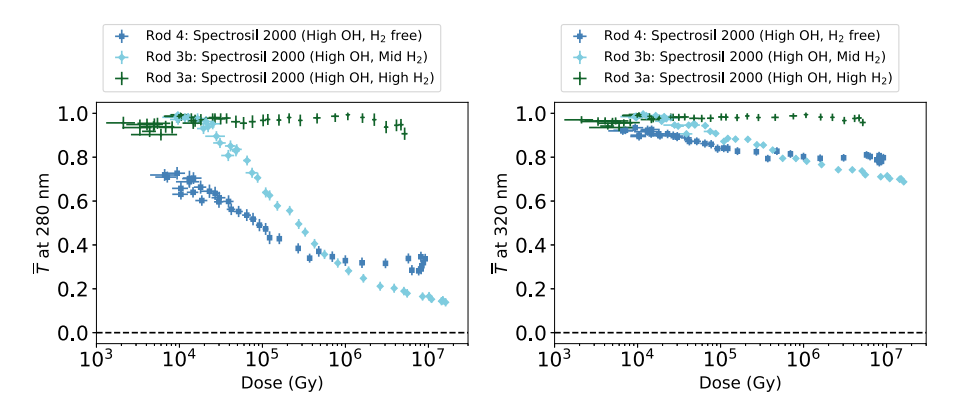


Fig. B.15. Comparison of the transmittance at 280 nm (left) and 320 nm (right) between Rod 4 (Spectrosil 2000, High OH and H₂ free), Rod 3b (Spectrosil 2000, High OH and Mid H₂), and Rod 3a (Spectrosil 2000, High OH and High H₂) at different dose levels.

References

- D. Milam, Review and assessment of measured values of the nonlinear refractive-index coefficient of fused silica, Appl. Opt. 37 (3) (1998) 546-550.
- $\hbox{\cite{beta} I.a. Miller, Optical Fiber Telecommunications, Elsevier, 2012.}$

- [3] C.D. Marshall, J.A. Speth, S.A. Payne, Induced optical absorption in gamma, neutron and ultraviolet irradiated fused quartz and silica, J. Non-Crystal. Solids 212 (1) (1997) 59–73.
- [4] L. Skuja, M. Hirano, H. Hosono, K. Kajihara, Defects in oxide glasses, Phys. Status Solidi (C) 2 (1) (2005) 15–24.
- [5] F. Nürnberg, B. Kühn, A. Langner, M. Altwein, G. Schötz, R. Takke, S. Thomas,

- J. Vydra, Bulk damage and absorption in fused silica due to high-power laser applications, in: Laser-Induced Damage in Optical Materials: 2015, Vol. 9632, International Society for Optics and Photonics, 2015, p. 96321R.
- [6] R. Brueckner, Properties and structure of vitreous silica. I, J. Non-Crystal. Solids 5 (2) (1970) 123–175.
- [7] N. Akchurin, R. Wigmans, Quartz fibers as active elements in detectors for particle physics, Rev. Sci. Instrum. 74 (6) (2003) 2955–2972.
- [8] Data and Properties Optics fused silica, Heraeus, URL https://www.heraeus.com/media/media/hca/doc_hca/products_and_solutions_8/optics/Data_and_Properties_Optics_fused_silica_EN.pdf.
- [9] R. Weeks, C. Nelson, Trapped electrons in irradiated quartz and silica: II, electron spin resonance, J. Am. Ceram. Soc. 43 (8) (1960) 399–404.
- [10] D.L. Griscom, Optical properties and structure of defects in silica glass, J. Ceram. Soc. Japan 99 (1154) (1991) 923–942.
- [11] D. Griscom, γ and fission-reactor radiation effects on the visible-range transparency of aluminum-jacketed, all-silica optical fibers, J. Appl. Phys. 80 (4) (1996) 2142–2155.
- [12] J.A. Salem, Transparent armor ceramics as spacecraft windows, J. Am. Ceram. Soc. 96 (1) (2013) 281–289.
- [13] B. Bilki, Y. Onel, Design, construction and commissioning of the upgrade radiation damage monitoring system of the CMS hadron forward calorimeters, in: 2018 IEEE Nuclear Science Symposium and Medical Imaging Conference Proceedings, NSS/MIC, 2018, pp. 1–4, http://dx.doi.org/10.1109/NSSMIC.2018. 8824611
- [14] N. Akchurin, N. Bartosik, J. Damgov, F. De Guio, G. Dissertori, E. Kendir, S. Kunori, T. Mengke, F. Nessi-Tedaldi, N. Pastrone, et al., Cerium-doped fused-silica fibers for particle physics detectors, J. Instrum. 15 (03) (2020) C03054.
- [15] S. Abdullin, V. Abramov, B. Acharya, M. Adams, N. Akchurin, U. Akgun, E. Anderson, G. Antchev, M. Arcidy, S. Ayan, et al., Design, performance, and calibration of CMS forward calorimeter wedges, Eur. Phys. J. C 53 (1) (2008) 139–166.
- [16] L. Evans, P. Bryant, LHC machine, J. Instrum. 3 (08) (2008) S08001.
- [17] The HL-LHC Project: High Luminosity Large Hadron Collider, URL https:// hilumilhc.web.cern.ch/.
- [18] G. Apollinari, O. Brüning, T. Nakamoto, L. Rossi, High luminosity large hadron collider HL-LHC, 2017, arXiv preprint arXiv:1705.08830.
- [19] P. Santos Díaz, F.S. Galan, R. De Maria, E. Kepes, P. Steinberg, R. Longo, S. Mazzoni, F. Cerutti, M. Sabate Gilarte, A. Infantino, B. Salvant, M. Murray, O. Boettcher, J. Hansen, V. Baglin, N. Zelko, E. Bravin, H. Mainaud, P. Bestmann, A. Herty, P. Fessia, M. Gonzalez de la Aleja Cabana, Mechanical and thermal design of the target neutral beam absorber for the high-luminosity LHC upgrade, Phys. Rev. Accel. Beams 25 (2022) 053001, http://dx.doi.org/10.1103/PhysRevAccelBeams.25.053001, URL https://link.aps.org/doi/10.1103/PhysRevAccelBeams.25.053001.
- [20] G. Aad, E. Abat, J. Abdallah, A. Abdelalim, A. Abdesselam, B. Abi, M. Abolins, H. Abramowicz, E. Acerbi, B. Acharya, et al., The ATLAS experiment at the CERN large hadron collider, J. Instrum. 3 (2008) S08003.
- [21] S. Chatrchyan, G. Hmayakyan, V. Khachatryan, CMS Collaboration, et al., The CMS experiment at the CERN LHC, J. Instrum. 3 (8) (2008) S08004.

- [22] H.S. Matis, M. Placidi, A. Ratti, W.C. Turner, E. Bravin, R. Miyamoto, The BRAN luminosity detectors for the LHC, Nucl. Instrum. Methods A 848 (2017) 114–126, http://dx.doi.org/10.1016/j.nima.2016.12.019, arXiv:1612.01238.
- [23] P. Jenni, M. Nessi, M. Nordberg, Zero degree calorimeters for ATLAS, in: Tech. rep, CM-P00072881, 2007.
- [24] O.A. Grachov, M. Murray, A.S. Ayan, P. Debbins, E. Norbeck, Y. Onel, D. d'Enterria, CMS Collaboration, Status of zero degree calorimeter for CMS experiment, in: AIP Conference Proceedings, Vol. 867, No. 1, American Institute of Physics, 2006, pp. 258–265.
- [25] A Radiation-Hard Zero Degree Calorimeter for ATLAS in the HL-LHC era, ATLAS Collaboration, 2021.
- [26] FLUKA CERN website https://fluka.cern.
- [27] C. Ahdida, et al., New capabilities of the FLUKA multi-purpose code, Front. Phys. 9 (2021) 788253, http://dx.doi.org/10.3389/fphy.2021.788253.
- [28] G. Battistoni, et al., Overview of the FLUKA code, Ann. Nucl. Energy 82 (2015) 10–18, http://dx.doi.org/10.1016/j.anucene.2014.11.007.
- [29] Quartz glass for optics data and properties, 2019, URL https://www.heraeus.com/media/hca/doc_hca/products_and_solutions_8/optics/Data_and_Properties_Optics_fused_silica_EN.pdf.
- [30] S. Yang, et al., ²²Na activation level measurements of fused silica rods in the LHC target absorber for neutrals compared to simulations, Phys. Rev. Accel. Beams 25 (9) (2022) 091001, http://dx.doi.org/10.1103/PhysRevAccelBeams.25.091001, arXiv:2204.01937.
- [31] R.G. Alía, M. Brugger, F. Cerutti, S. Danzeca, A. Ferrari, S. Gilardoni, Y. Kadi, M. Kastriotou, A. Lechner, C. Martinella, et al., LHC and HL-LHC: Present and future radiation environment in the high-luminosity collision points and RHA implications, IEEE Trans. Nucl. Sci. 65 (1) (2017) 448–456.
- [32] D. Prelipcean, Comparison between measured radiation levels and FLUKA simulations at CHARM and in the LHC tunnel of P1-5 within the R2E project in run 2. vergleich zwischen gemessenen strahlungswerten und FLUKA-simulationen bei CHARM undim LHC-tunnel von P1-5 innerhalb des R2E-projekts in run 2, 2021, URL https://cds.cern.ch/record/2777059. Presented 29 Jul 2021.
- [33] Luminosity public results Run2, 2020, https://twiki.cern.ch/twiki/bin/view/ AtlasPublic/LuminosityPublicResultsRun2. (Accessed 23 December 2020).
- [34] Data sheet of refractive index liquid series AA, 2018, URL https: //cargille.com/wp-content/uploads/2018/10/Refractive-Index-Liquid-Series-AA-n-1.4560-at-589.3-nm-and-25%C2%AFC.pdf.
- [35] Agilent Cary 4000/5000/6000i Series UV-VIS-NIR Spectrophotometers, URL https://www.agilent.com/cs/library/brochures/5990-7786EN_Cary-4000-5000-6000i-UV-Vis-NIR_Brochure.pdf.
- [36] D.F. Swinehart, The beer-lambert law, J. Chem. Educ. 39 (7) (1962) 333.
- 37] A. Höpe, Diffuse reflectance and transmittance, in: Experimental Methods in the Physical Sciences, Vol. 46, Elsevier, 2014, pp. 179–219.
- [38] K. Hamamatsu Photonics, Photomultiplier tubes and assemblies for scintillation counting & high energy physics, 2017, Web (Accessed Date 14 September 2020): R8055 R7250 Datasheet.
- [39] B. Kühn, E. Arnold, H.-D. Witzke, F.-J. Schilling, M. Stamminger, B. Uebbing, Boundary conditions for the saturation and amplitude of induced absorption in synthetic fused silica, in: 8th Symposium SiO2, Advanced Dielectrics and Related Devices, Varenna, Italy, 2010.